Three-mode coupling interference patterns in the dynamic structure factor of a relaxor ferroelectric

M. E. Manley,[1,*] D. L. Abernathy,[2] R. Sahul,[3] P. J. Stonaha,[1] and J. D. Budai[1]
[1]*Materials Science and Technology Division, Oak Ridge National Laboratory, Oak Ridge, Tennessee 37831, USA*
[2]*Quantum Condensed Matter Division, Oak Ridge National Laboratory, Oak Ridge, Tennessee 37831, USA*
[3]*TRS Technologies, State College, Pennsylvania 16801, USA*
(Received 26 February 2016; published 22 September 2016)

A longstanding controversy for relaxor ferroelectrics has been the origin of the "waterfall" effect in the phonon dispersion curves, in which low-energy transverse phonons cascade into vertical columns. Originally interpreted as phonons interacting with polar nanoregions (PNRs), it was later explained as an interference effect of coupling damped optic and acoustic phonons. In light of a recently discovered PNR vibrational mode near the "waterfall" wave vector [M. E. Manley, J. W. Lynn, D. L. Abernathy, E. D. Specht, O. Delaire, A. R. Bishop, R. Sahul, and J. D. Budai, Nat. Commun. **5**, 3683 (2014)], we have reexamined this feature using neutron scattering on [100]-poled PMN-30%PT [$0.6Pb(Mg_{1/3}Nb_{2/3})O_3 - 0.3PbTiO_3$]. We find that the PNR mode couples to both optic and acoustic phonons and that this results in complex patterns in the dynamic structure factor, including intensity pockets and peaks localized in momentum-energy space. These features are fully explained by extending the mode-coupling model to include three coupled damped harmonic oscillators representing the transverse optic, acoustic, and PNR modes.

DOI: 10.1103/PhysRevB.94.104304

I. INTRODUCTION

Crystal lattice dynamics are normally well described by harmonic dispersion curves that are broadened to account for the finite lifetimes of the phonons. Shortened phonon lifetimes are caused by anharmonic phonon-phonon [1], electron-phonon [2], and/or disorder [3] induced phonon scattering and can normally be modeled using uncoupled damped harmonic oscillators. Important exceptions include intrinsic localized modes (a.k.a. discrete breathers) resulting from strong anharmonicity [4–9] and Anderson localized modes resulting from a high degree of disorder [10–12]. Another exception is the so-called "waterfall" effect in phonon dispersion curves, in which the measured phonon dispersion cascades into vertical columns of intensity at particular wave vectors [13]. The "waterfall" effect is not fully understood but has been observed in several technologically important materials, including relaxor ferroelectric actuator materials [13–19], conventional ferroelectrics [20], and in a strongly anharmonic thermoelectric material [21]. Because the feature was first identified in a relaxor ferroelectric material [13] and because the "waterfall" wave vectors appear to be matched to the size of polar nanoregions (PNRs) [13], it was originally proposed that the "waterfall" effect results from an interaction between the phonons and PNRs [13]. However, because the effect also appears in materials not bearing PNRs and because the "waterfall" wave vector depends on which Brillouin zone is measured, doubt was cast on this interpretation [22]. A simple alternative model proposed by Hlinka *et al.* [22] explains the "waterfall" effect and its dependence on Brillouin zone in terms of two-mode coupling between damped transverse optic (TO) and transverse acoustic (TA) phonons, without the need for PNRs.

Recently, however, an extra vibrational mode associated with PNRs was found to exist between the TO and TA phonons in relaxor ferroelectrics PMN-30%PT [$0.6Pb(Mg_{1/3}Nb_{2/3})O_3 - 0.3PbTiO_3$] and PZN-5%PT [$0.95Pb(Zn_{1/3}Nb_{2/3})O_3 - 0.05PbTiO_3$] [12]. Above the Curie temperature ($T_C = 405$ K for PMN-30%PT) the PNR mode appears well localized (dispersionless) and merges with the TO phonon near $\boldsymbol{q} = 0.2$ reciprocal lattice units [12], which is close to the "waterfall" wave vector [16,17]. Below T_C the PNR mode avoids crossing the TO phonon by bending downward towards the zone center and into the "waterfall" feature [12]. The avoided crossing can be understood in terms of a linear coupling of the PNR vibrational modes and the transverse phonons [23]. It was also shown that coupling of PNRs to the TA phonons induces a large shear softening in the [110]-TA phonon [24]. This is the same shear softening known to enable the giant electromechanical coupling in relaxor-based ferroelectrics, which have revolutionized sensor and ultrasound applications [25]. Hence, understanding the coupling of PNR modes to transverse phonons is central to the most technologically important property of relaxor ferroelectrics [25]. In this article, we investigate the anharmonic contribution to this coupling by observing the "waterfall" feature interact with the PNR vibrational mode [12] using inelastic neutron scattering. We make use of the fact that the PNR modes align with [100] poling [26] to isolate the effects of the PNR mode in PMN-30%PT. Perpendicular to the poling direction no PNR mode appears, and the two-mode coupling model proposed by Hlinka *et al.* [22] fully captures the waterfall feature. Along the poling direction, however, the PNR mode appears more intense [26] and couples anharmonically to both the TO and TA phonons. The resulting three-mode anharmonic coupling produces complex dynamical features, including intensity pockets and peaks localized in small regions of momentum-energy space. These features are fully explained by an expanded version of the Hlinka model [22] that includes three coupled damped harmonic oscillators representing the TO, PNR, and TA modes. The damping models phonon lifetime broadening resulting from anharmonic phonon-phonon scattering and disorder scattering, while the coupling accounts for mode

*manleyme@ornl.gov

synchronization effects resulting from mode coupling. The combined effect of damping (broadening) and coupling create the complex patterns in the dynamic structure factor. To explain the presence of strong damping in all three modes, we note that in addition to disorder there are three distinct instabilities: (i) a soft anharmonic TO phonon related to the ferroelectric instability [27], (ii) a soft anharmonic TA phonon related to a shear instability associated with the nearby morphotropic phase boundary [28], and (iii) for the PNR mode there is a local Pb atom off-centering instability [29,30].

II. EXPERIMENT

Single-crystal boules of PMN-PT were grown using a modified Bridgman growth method (http://www.trstechnologies.com/Materials/single_crystals.php). The boules were oriented for the major crystallographic orientations $[001]_c$, $[011]_c$, and $[[111]_c$ using a Laue x ray and x-ray diffractometry. Sections of crystals 0.5 cm thick were sliced from the ~5 cm diameter boule using an one-dimensional saw. The composition of the crystal, PMN-30%PT, was first estimated from the positions in the crystal boule and then later confirmed by measuring the transition temperatures using high-temperature x-ray diffraction on the individual crystals and comparing these to the known phase diagrams using a method described in detail elsewhere [12]. For poling, two 0.5-cm-thick ~5-cm- diameter slices were cleaned and metallized with an ~500-Å layer of chromium and 2000-Å layer of gold using a sputtering process. The metallized section was then poled using a polarization bath. The crystal slice is immersed in a bath of Fluorinert oil (silicone oil with a high dielectric strength) and a dc electric field is applied. For the rhombohedral PMN-30%PT crystal, the crystal samples were poled by application of a dc electric field of 4 kV/cm at room temperature. The piezoelectric charge coefficient (d_{33}) was measured using a d_{33} meter to determine if the crystal slices were poled into a piezoelectric state. After poling, polarization changes as the function of applied electric field were observed on batch qualification samples using a hysteresis loop device that works based on a Sawyer-Tower circuit. This measurement uses an integrator to determine the charge per unit area formed on the electroded surface of a dielectric subjected to an electric field. The voltage is applied in the form of a biased (unipolar) triangle wave (0 to peak) for a small number of cycles (~3). The hysteresis area between the field ascending and field descending portions of the curve is proportional to the energy lost as heat during a charge-discharge cycle, and this hysteresis loop represents characteristic behavior that is typical of ferroelectric materials.

Inelastic neutron-scattering measurements were performed on the large (~20 cm^3 for two stacked 0.5-cm-thick plates) [100]-poled PMN-30%PT crystal using the Angular-Range Chopper Spectrometer (ARCS) at the Spallation Neutron Source of Oak Ridge National Laboratory [31]. Measurements where performed at room temperature with an incident neutron energy of 25 meV and with the crystal oriented in the $(HK0)$ plane. Comprehensive four-dimensional $\boldsymbol{Q}$-E volumes of data were obtained by rotating the angle between the [100] axis and the incident beam in 0.5-degree steps and combining the data using MSLICE in the Data Analysis and Visualization Environment (DAVE) software [32]. Data were collected at each angle from –70 to 55 deg to obtain a complete data set that includes $\boldsymbol{Q}$ values in directions both perpendicular to and parallel to the [100]-poling direction in the $(HK0)$ plane.

III. CALCULATIONS

Mode-coupling calculations were performed for models containing either two or three coupled damped harmonic oscillators representing the TO and TA modes, or the TO, PNR, and TA modes, respectively. For two-mode coupling the model described by Hlinka *et al.* [22], which involves 2×2 matrices, is used directly. For three-mode coupling the model is expanded to 3×3 matrices as follows: The dynamical matrix $\mathbf{D}_q$ is defined as

$$\mathbf{D}_q = \begin{pmatrix} \omega_{\mathrm{TA}}^2(q) & \Delta_{\mathrm{AP}}(q) & \Delta_{\mathrm{AO}}(q) \\ \Delta_{\mathrm{AP}}(q)^* & \omega_{\mathrm{PNR}}^2(q) & \Delta_{\mathrm{OP}}(q) \\ \Delta_{\mathrm{AO}}(q)^* & \Delta_{\mathrm{OP}}(q)^* & \omega_{\mathrm{TO}}^2(q) \end{pmatrix}, \tag{1}$$

where $\omega_{\mathrm{TA}}(q)$, $\omega_{\mathrm{PNR}}(q)$, and $\omega_{\mathrm{TO}}(q)$ represent the bare TA, PNR, and TO mode dispersion curves, with q being the reduced phonon wave vector. The off-diagonal terms $\Delta_{\mathrm{AP}}(q)$, $\Delta_{\mathrm{AO}}(q)$, and $\Delta_{\mathrm{OP}}(q)$ describe the bilinear interaction [22] between the TA and PNR (AP), TA and TO (AO), and TO and PNR (OP) modes, respectively. For simplicity, in this paper these off-diagonal interaction terms are assumed to be all the same and are set equal to the single off-diagonal interaction term used in the two-mode coupling model [22]. The damping matrix is

$$\boldsymbol{\Gamma}_q = \begin{pmatrix} \Gamma_{\mathrm{TA}}(q) & \Gamma_{\mathrm{AP}}(q) & \Gamma_{\mathrm{AO}}(q) \\ \Gamma_{\mathrm{AP}}(q) & \Gamma_{\mathrm{PNR}}(q) & \Gamma_{\mathrm{OP}}(q) \\ \Gamma_{\mathrm{AO}}(q) & \Gamma_{\mathrm{OP}}(q) & \Gamma_{\mathrm{TO}}(q) \end{pmatrix}, \tag{2}$$

where $\Gamma_{\mathrm{TA}}(q)$, $\Gamma_{\mathrm{PNR}}(q)$, and $\Gamma_{\mathrm{TO}}(q)$ are the bare-mode-frequency–independent damping [22], and the off-diagonal terms $\Gamma_{\mathrm{AP}}(q)$, $\Gamma_{\mathrm{AO}}(q)$, and $\Gamma_{\mathrm{OP}}(q)$ are the viscous interaction terms [22]. Using the same approximation used in the two-mode coupling model of Ref. [22], the viscous interaction terms are all assumed to be negligibly small, so $\Gamma_{\mathrm{AP}}(q) = \Gamma_{\mathrm{AO}}(q) = \Gamma_{\mathrm{OP}}(q) = 0$. The inelastic neutron-scattering spectrum in the high-temperature limit ($k \gg \hbar\omega$) is given by [22]

$$I(\omega,q) = kT\omega^{-1}\mathbf{f}(q)^*\mathrm{Im}[\mathbf{G}(\omega,q)]\mathbf{f}(q), \tag{3}$$

$$\mathbf{G}(\omega,q) = \left(\mathbf{D}_q - i\omega\boldsymbol{\Gamma}_q - \omega^2\mathbf{E}\right)^{-1}, \tag{4}$$

where $\mathbf{E}$ is a 3×3 unit matrix, and $\mathbf{f}(q)$ is a three-component vector characterizing the structure factors of the bare TA, PNR, and TO modes. In this paper the dispersion in the waterfall is sliced into sections showing the out-of-plane direction along $\boldsymbol{Q} = [0,0,L]$ for $\boldsymbol{Q} = [2,K,0](K = 0.2,0.3,$ and $0.4)$ in order to give a higher-dimensional view of the feature. Along L the bare dispersion curves are well described using

$$\omega_{\mathrm{TA}}^2(q) = A + B\sin^2(\pi q), \tag{5}$$

$$\omega_{\mathrm{PNR}}^2(q) = C + D\sin^2(\pi q), \tag{6}$$

$$\omega_{\mathrm{TO}}^2(q) = E + F\sin^2(\pi q), \tag{7}$$

$$\Delta_{\mathrm{AP}}(q) = \Delta_{\mathrm{AO}}(q) = \Delta_{\mathrm{OP}}(q) = d\sin^2(\pi q), \tag{8}$$

where A, B, C, D, E, and F define the shape of the bare dispersion curves and d describes the strength of the mode mixing [22]. The bare-mode independent damping terms

$\Gamma_{TA}(q)$, $\Gamma_{PNR}(q)$, and $\Gamma_{TO}(q)$ are fixed at constant values along the out-of-plane direction. To account for the strong q dependence of the structure factor for the PNR and TO modes, the structure factors are modeled using

$$\mathbf{f}(q) = \begin{pmatrix} f_{TA} \\ f_{PNR}[1 - \sin^2(\pi q)] \\ f_{TO}[1 - \sin^2(\pi q)] \end{pmatrix}, \quad (9)$$

where f_{TA}, f_{PNR}, and f_{TO} are dimensionless factors that account for the differences in structure factors between the TA, PNR, and TO modes, respectively.

IV. RESULTS

Figure 1 shows image plots of both the in-plane and out-of-plane dispersion of the TO, PNR, and TA phonons measured on the ARCS spectrometer on [100]-poled PMN-30%PT at 300 K. The in-plane dispersion of all three modes in Fig. 1(a) can be seen to repeat in going from zone to zone along $\boldsymbol{Q} = [2,K,0]$, with maxima occurring at the zone boundaries at $K = +0.5$ and -0.5 (X points) and minima at the zone centers at $K = -1,0$, and 1 (Γ points). The dispersion of the TO, PNR, and TA modes are in good agreement with those measured on a triple-axis spectrometer on the same PMN-30%PT crystal at the same temperature (300 K) in Ref. [12]. The TO and TA phonon dispersion are also similar to those measured previously in PMN-32%PT [33,34]. An extra-soft optic mode was also identified previously in PMN [35–37], but that mode only appears at high temperatures [36] and was only at wave vectors near the zone center beneath the TO mode. By contrast, the PNR mode identified here is observed dispersing across multiple zones (Fig. 1) and at a wide range of temperatures, including below T_C (~405 K), between T_C and the Burns temperature ($T_d \approx 650$ K), and above T_d [12]. The appearance of an isolated splitting in the TO phonon near the zone center needs to be considered with care. The reason is that recent experimental and theoretical work shows that a similar feature can emerge owing to an anharmonic contribution to the phonon self-energy [38]. In this case, although the splitting of the TO phonon may be real and temperature dependent; it only appears in a narrow region of reciprocal space and does not represent a true extra-soft mode [38].

Ferroelectric domains introduce a crystal mosaic that releases the extinction of Bragg scattering, which leads to more prominent spurious scattering effects that need to be carefully avoided or corrected. At high temperatures, where the PNR local mode was first observed [12], Bragg extinction happens because the angular acceptance for Bragg diffraction is much narrower than the ~0.6-deg incident neutron beam divergence on the ARCS instrument. With the formation of ferroelectric domains, however, the angular acceptance for diffraction expands and Bragg scattering intensities increase by about a factor of 20 for our crystal on the ARCS instrument. This has the effect of enhancing parasitic scattering effects (depletion of the primary beam by diffraction) and accidental multiple scattering processes. The dashed red lines in Fig. 1 indicate data collected at constant crystal angles corresponding to various Bragg diffraction conditions. Because the Bragg scattering is strong, the incident neutron beam suffers a ~15%

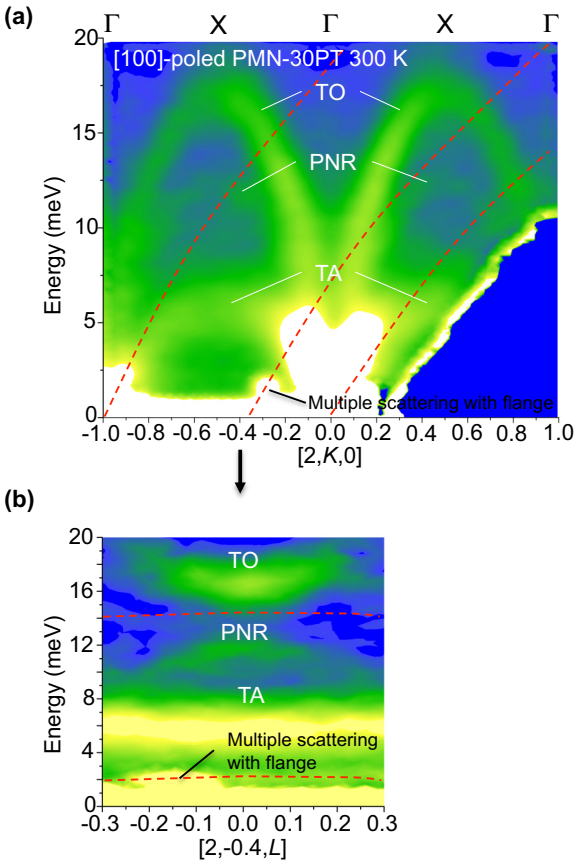

FIG. 1. Inelastic neutron-scattering measurements of the phonon dispersion curves for [100]-poled PMN-30%PT. (a) In-plane dispersion along $\boldsymbol{Q} = [2,K,0]$, which selects for transverse modes with atom displacements parallel to the [100] poling direction. The TO, PNR, and TA mode dispersion curves form arcs that are symmetric with respect to positive and negative values of K, and all three peak at the zone boundaries at $K = +0.5$ and -0.5. The red lines indicate the trajectories of data collected at fixed crystal angles corresponding to Bragg conditions. These trajectories do not follow the crystal symmetry (see text). (b) Out-of-plane dispersion along $\boldsymbol{Q} = [2,-0.4,L]$. The TO, PNR, and TA modes are symmetric with respect to positive and negative values of L. The multiple scattering with flange features is a spurious scattering effect and is not symmetric with respect to positive and negative values of L. These slices of the data, and other similar ones, are used to separate real features from spurious effects.

loss of intensity after it travels through the crystal at the (200) Bragg angle, and this reduces the scattered intensity for all data collected at this angle. The result is an intensity shadow running along the dashed red line crossing (200), and similar intensity shadows occur for the other dashed red lines. Any accidental Bragg–first multiple scattering process involving one these particular crystal angles must also fall on one of the dashed red lines. Unlike real excitations, these lines to do not conform to the symmetry of the crystal when viewed across multiple zones, so artifacts can be easily separated from real modes. Also, the equivalent parasitic scattering lines are very different on a triple-axis spectrometer (which uses fixed final neutron energy rather than fixed incident neutron energy), yet the TO, PNR, and TA modes all appear the same

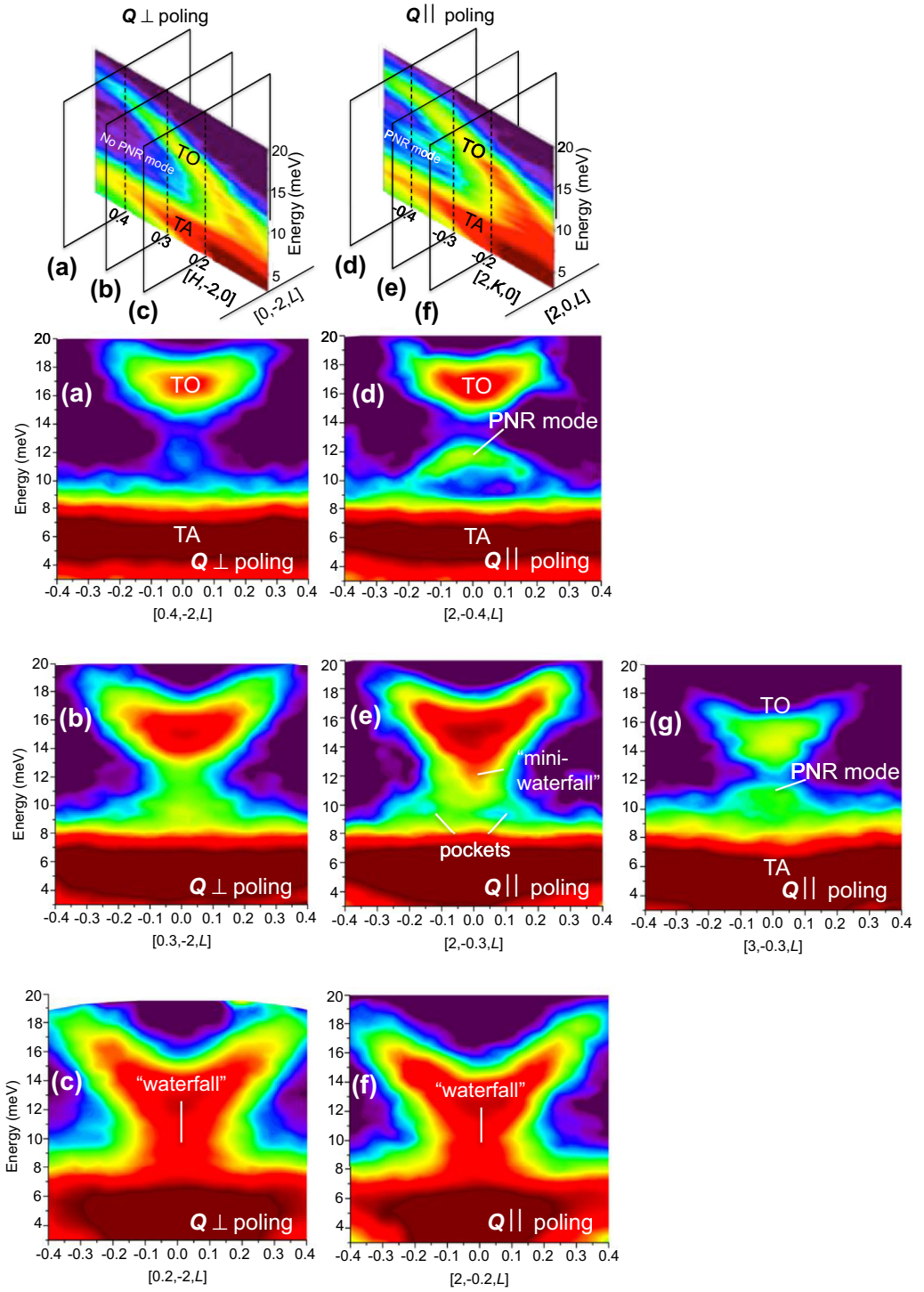

FIG. 2. Inelastic neutron scattering of the "waterfall" feature sliced into out-of-plane sections in energy-momentum space. The in-plane image plots shown for reference at the top are after Ref. [26]. (a)–(c) Perpendicular to the poling direction, near $(0, -2, 0)$, no PNR mode [12] is detected between the TO and TA modes and a single "waterfall" feature appears. (d)–(f) Along the poling direction, near (200), a separate PNR mode appears between the TO and TA modes. (e) A "mini-waterfall" feature appears between the TO and PNR mode. (f) TO-TA coupling dominates the main "waterfall" feature. (g) "Mini-waterfall" appearance changes in (300) zone.

[12]. The PNR mode dispersion can also be observed in the out-of-plane direction along $\boldsymbol{Q} = [2, -0.4, L]$ in Fig. 1(b). A multiple scattering feature coming from a diffracted beam scattering off of a flange located above the crystal during the measurement can also be seen at around 2 meV. Although this is elastic multiple scattering, it appears at a finite energy because the increased path length mimics the time delay of a neutron inelastic event on a time-of-flight instrument.

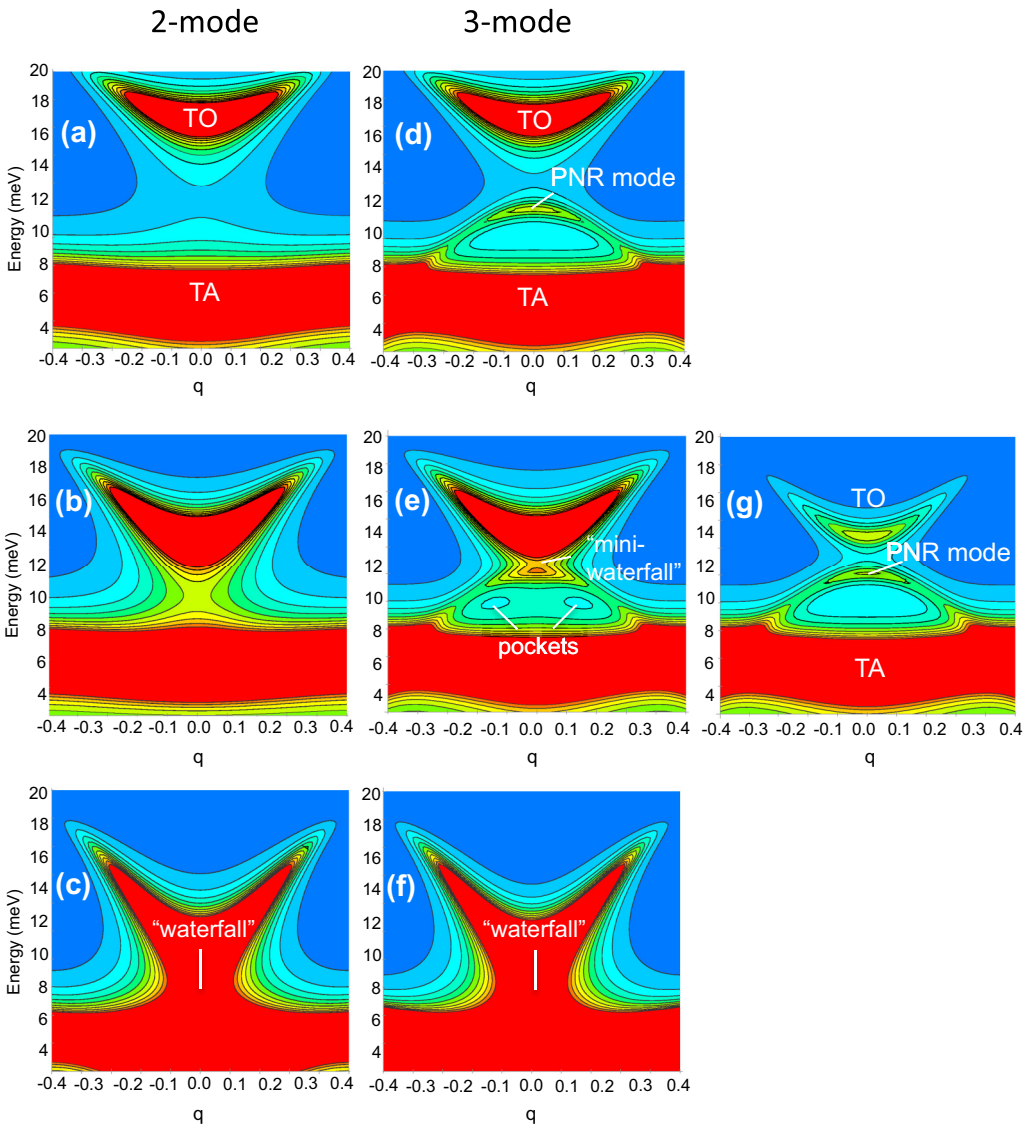

FIG. 3. Mode-coupling model calculations describing the "waterfall" feature sliced into out-of-plane sections in energy-momentum space in Fig. 2 (see text for details). The panels (a)–(g) correspond to the experimental results with the same labels shown in Fig. 2.

This scattering process was positively identified during the experiment by eliminating it by covering the flange with a neutron absorber (cadmium foil). Note again that, unlike the real modes, this accidental multiple scattering does not follow the crystal symmetry. The feature appears at $L = -0.15$ but not at $L = +0.15$. To avoid spurious scattering effects in the following analysis, we chose the region between $K = -0.4$ and $K = -0.2$ ($\boldsymbol{Q} = [2, K, L]$) at energies above ~3 meV to investigate the role of the PNR mode on the "waterfall" feature in the phonon dispersion.

The image plots shown in Fig. 2 display the waterfall feature sliced into out-of-plane sections, viewed both perpendicular [Figs. 2(a)–2(c)] and parallel [Figs. 2(d)–2(g)] to the [100] poling direction of the PMN-30%PT crystal. Perpendicular to the poling direction, near (0,–2,0), no PNR mode [12] is detected between the TO and TA modes. In the $\boldsymbol{Q} = [0.4, -2, L]$ slice [Fig. 2(a)], the TO and TA modes appear separated with only a weak vertical column of intensity extending between them near $L = 0$. Moving toward the zone center, the modes become closer in energy and the $\boldsymbol{Q} = [0.3, -2, L]$ slice [Fig. 2(b)] shows a more intense vertical column extending between the TO and TA modes. In the $\boldsymbol{Q} = [0.2, -2, L]$ slice [Fig. 2(c)], the vertical column becomes comparable in intensity to the modes themselves. Figure 2(c) exhibits a fully formed waterfall feature, since the two modes are no longer clearly separated near $L = 0$. Along the poling direction, near (200), a separate PNR mode is clearly observed between the TO and TA modes in the $\boldsymbol{Q} = [2, -0.4, L]$ slice [Fig. 2(d)]. The main difference between Figs. 2(a) and 2(d) is the presence of the PNR mode [12,26]. On moving toward the zone center, the PNR mode couples to both the TO and TA phonons, see the $\boldsymbol{Q} = [2, -0.3, L]$ slice in Fig. 2(e). The three-mode coupling results in some unusual features in the dynamic structure, including intensity pockets localized in

TABLE I. Mode-coupling parameters used in the calculations of the inelastic intensities displayed in Fig. 3. See Eqs. (5)–(7) for the meanings of mode shaping parameters, *A*–*F*, and Eq. (8) for the meaning of the coupling parameter, *d*. The parameters Γ_{TA}, Γ_{PNR}, and Γ_{TO} are the values of the bare mode damping, and f_{TA}, f_{PNR}, and f_{TO} are the scale parameters for the structure factors, Eq. (9).

Parameter	(*a*)	(*b*)	(*c*)	(*d*)	(*e*)	(*f*)	(*g*)
A (meV^2)	35	35	20	35	35	20	35
B (meV^2)	10	10	10	10	10	10	10
C (meV^2)	N/A	N/A	N/A	135	135	36	135
D (meV^2)	N/A	N/A	N/A	−107	−107	−27	−107
E (meV^2)	290	195	120	290	195	120	195
F (meV^2)	150	200	250	150	200	250	200
d (meV^2)	10	10	10	10	10	10	10
Γ_{TA} (meV)	1	1	1	1	1	1	1
Γ_{PNR} (meV)	N/A	N/A	N/A	1	1	1	1
Γ_{TO} (meV)	1.4	1.4	1.4	1.4	1.4	1.4	1.4
f_{TA}	0.7	0.7	0.7	0.7	0.7	0.7	0.7
f_{PNR}	N/A	N/A	N/A	0.25	0.25	0.25	0.25
f_{TO}	1	1	1	1	1	1	0.4

small regions of momentum-energy space [see Fig. 2(e)] and a "mini-waterfall" feature that extends between the TO and PNR mode in Fig. 2(e). Along with the mini-waterfall comes a focus of the intensity of the PNR mode near $\boldsymbol{Q} = [2,-0.3,0]$. As with the usual waterfall effect this mini-waterfall effect depends on the structure factor of the TO phonon [22] and therefore appears different in the (300) zone [Fig. 2(g)] than in the (200) zone [Fig. 2(e)]. All of these features can be explained by the mode-coupling calculations shown in Fig. 3.

Perpendicular to the poling direction where no PNR mode appears, the two-mode coupling model of the type proposed by Hlinka *et al.* [22] captures the basic waterfall features; compare the neutron experiments in Figs. 2(a)–2(c) with the related mode-coupling calculations in Figs. 3(a)–3(c). To obtain the basic "waterfall" behavior, the coupling and damping parameters are held fixed while the modes are simply brought closer together according to the experimental dispersion. The two-mode structure factors, coupling, and damping parameters are listed in Table I.

Parallel to the poling direction the PNR mode clearly appears [Fig. 2(d)] and exhibits coupling to the TO and TA phonons [Fig. 2(e)], and this can be described by the three-mode coupling model [Figs. 3(d)–3(f)]. With well-separated modes at $\boldsymbol{Q} = [2,-0.4,L]$ [Fig. 2(d)], the three-mode coupling model shown in Fig. 3(d) captures the following features: The TO, PNR, and TA modes all appear distinct, with a weak diffuse intensity extending between all three modes [compare Fig. 2(d) and Fig. 3(d)]. As the modes become closer at $\boldsymbol{Q} = [2,-0.3,L]$ [Fig. 2(e)], the three-mode coupling model shown in Fig. 3(e) shows a mini-waterfall extending between the TO and PNR mode, the intensity of the PNR mode is concentrated near $L = 0$, and intensity pockets appear near $q = +/-0.125$ [compare Fig. 3(e) with Fig. 2(e)]. To obtain these features in the three-mode coupling model, the TO mode is just moved closer to the PNR modes; no changes in the coupling parameters are necessary (see parameters listed in Table I). As the three modes become even closer at $\boldsymbol{Q} = [2,-0.2,L]$ [Fig. 2(f)], the three-mode coupling captures the feature, which is a full waterfall [compare Fig. 3(f) with Fig. 2(f)]. In this case, the PNR mode is not observable in the data. To estimate the position of the PNR mode in the three-mode coupling calculation, we used the value observed for unpoled PMN-30%PT in Ref. [12], which is 9.2 meV. However, because the TO-TA coupling dominates the structure in this case, the appearance of the waterfall feature is not sensitive to the position of the PNR mode in Fig. 3(f). To demonstrate that it is the reduction of the structure factor that reveals the almost bare PNR mode in Fig. 2(g) compared to Fig. 2(e), we reduced the TO structure factor in the three-mode coupling model shown in Fig. 3(g). All that is required to go from the complex structure in Fig. 3(e) to the three distinct modes in Fig. 3(g) is a reduction in the structure factor of the TO phonon (see parameters listed in Table I). Hence, the difference between the complex pattern in Fig. 2(e) [or model Fig. 3(e)] and Fig. 2(g) [or model Fig. 3(g)] is just the intensity of the TO phonon as modified by the structure factor.

V. DISCUSSION

The complex dynamical features emerging in PMN-30%PT reveal an unusually strong damping of three modes. While part of this is likely from disorder scattering, we identify three independent instabilities that likely drive strong anharmonicity in each of the modes separately. For the TO phonon there is the fact that the material is close to the ferroelectric transition temperature, at which point there is a soft-mode instability in the TO phonon near the zone center [27]. For the TA phonon we note that the composition is on the edge of the morphotropic phase boundary, and this has been shown to be associated with an elastic shear softening instability [28]. For the PNR mode we note that it originates with Pb atoms [12] that are unstable to local off-centering displacements [29]. This local instability has been shown theoretically to originate with an attraction of the Pb^{2+} atoms to underbonded O atoms resulting from variations in the local chemical environment [30]. It is this same local instability that allows the PNR modes to be aligned along [100] with poling [26].

The interference patterns emerging from this three-mode anharmonic coupling challenges conventional wisdom about how inelastic neutron-scattering spectra are analyzed and interpreted. In the conventional view, phonon dispersion curves are assumed to be smooth and continuous surfaces. Consequently, a feature appearing confined in a small region of reciprocal space is usually dismissed as spurious. On a triple-axis spectrometer, for example, it is customary to tilt the crystal out of plane to determine if a feature is part of a real dispersion curve or an artifact. The spectrum in Figs. 2(a)–2(g) are measured in the out-of-plane direction and are similar to doing tilt measurements. Tilting from the $\boldsymbol{Q} = [2,-0.4,0]$ point would be similar to the slice shown in Fig. 2(d). In this case, all three modes appear continuous out of the plane and therefore appear to be real dispersion curves. On the other hand, if the same tilting is done from the $\boldsymbol{Q} = [2,-0.3,0]$ point [Fig. 2(e)], the ∼11 meV feature's intensity quickly decreases, and this might be incorrectly dismissed as spurious. As shown in Fig. 3(e), however, this is a real feature that emerges from interference in the three-mode coupling model.

This is also confirmed by moving to the next zone out and tilting from $\boldsymbol{Q} = [3, -0.3, 0]$ [Fig. 2(g)]. Here, all three modes appear continuous again, and this is also evident in the relevant mode coupled calculation shown in Fig. 3(g). The model shows that it is the decrease in the structure factor of the TO mode in the (300) zone that allows the PNR mode dispersion to be observed. Similarly, the intensity pockets [Figs. 2(e) and 3(e)] may also be misinterpreted without including the damped three-mode coupling interference effects. The full four-dimensional $\boldsymbol{Q}$-E space view (three momentum + energy coordinates) afforded by the ARCS time-of-flight spectrometer, and other similar instruments, provides a distinct advantage in identifying these subtle multimode-coupling effects.

VI. CONCLUSION

The transverse lattice dynamics of PMN-30%PT exhibit complex patterns in the dynamic structure factor, including extra peaks and pockets localized in $\boldsymbol{Q}$-E space. The patterns emerge from interferences from coupling of three strongly damped modes. Two of the modes are the conventional transverse optic (TO) and transverse acoustic (TA) phonons, while the third arises from the local dynamics of polar nanoregions [12]. Strong anharmonicity likely appears in all three modes because of a collection of instabilities in both the average [27,28] and local structures [29,30]. These same instabilities also drive or enhance the technologically important giant electromechanical coupling in this material [26–28]. Hence, the process that optimized the ultrahigh piezoelectric response for applications [25] also produces complex patterns in the dynamic structure factor.

ACKNOWLEDGMENTS

Research sponsored by the U.S. Department of Energy, Office of Basic Energy Sciences, Materials Sciences and Engineering Division. The research performed at the Oak Ridge National Laboratory's Spallation Neutron Source was sponsored by the U.S. Department of Energy, Office of Basic Energy Sciences.

[1] R. A. Cowley, Rep. Prog. Phys. **31**, 123 (1968).
[2] F. Weber, L. Pintschovius, W. Reichardt, R. Heid, K.-P. Bohnen, A. Kreyssig, D. Reznik, and K. Hradil, Phys. Rev. B **89**, 104503 (2014).
[3] A. Gobel, D. T. Wang, M. Cardona, L. Pintschovius, W. Reichardt, J. Kulda, N. M. Pyka, K. Itoh, and E. E. Haller, Phys. Rev. B **58**, 10510 (1998).
[4] D. K. Campbell, S. Flach, and Y. S. Kivshar, Phys. Today **57**(1), 43 (2004).
[5] S. Flach and A. Gorbach, *Discrete Breathers–Advances in Theory and Applications* (Elsevier Science, New York, 2008).
[6] M. E. Manley, M. Yethiraj, H. Sinn, H. M. Volz, A. Alatas, J. C. Lashley, W. L. Hults, G. H. Lander, and J. L. Smith, Phys. Rev. Lett. **96**, 125501 (2006).
[7] M. E. Manley, A. J. Sievers, J. W. Lynn, S. A. Kiselev, N. I. Agladze, Y. Chen, A. Llobet, and A. Alatas, Phys. Rev. B **79**, 134304 (2009).
[8] M. E. Manley, D. L. Abernathy, N. I. Agladze, and A. J. Sievers, Sci. Rep. **1**, 4 (2011).
[9] M. E. Manley, J. R. Jeffries, H. Lee, N. P. Butch, A. Zabalegui, and D. L. Abernathy, Phys. Rev. B **89**, 224106 (2014).
[10] A. Lagendijk, B. van Tiggelen, and D. S. Wiersma, Phys. Today **62**(8), 24 (2009).
[11] C. Monthus and T. Garel, Phys. Rev. B **81**, 224208 (2010).
[12] M. E. Manley, J. W. Lynn, D. L. Abernathy, E. D. Specht, O. Delaire, A. R. Bishop, R. Sahul, and J. D. Budai, Nat. Commun. **5**, 3683 (2014).
[13] P. M. Gehring, S. E. Park, and G. Shirane, Phys. Rev. Lett. **84**, 5216 (2000).
[14] P. M. Gehring, S. E. Park, and G. Shirane, Phys. Rev. B **63**, 224109 (2001).
[15] I. Tomeno, S. Shimanuki, Y. Tsunoda, and Y. Y. Ishii, J. Phys. Soc. Jpn. **70**, 1444 (2001).
[16] S. Wakimoto, C. Stock, Z.-G. Ye, W. Chen, P. M. Gehring, and G. Shirane, Phys. Rev. B **66**, 224102 (2002).
[17] P. M. Gehring, S. Wakimoto, Z.-G. Ye, and G. Shirane, Phys. Rev. Lett. **87**, 277601 (2001).
[18] D. La-Orauttapong, B. Noheda, Z.-G. Ye, P. M. Gehring, J. Toulouse, D. E. Cox, and G. Shirane, Phys. Rev. B **65**, 144101 (2002).
[19] T. Y. Koo, P. M. Gehring, G. Shirane, V. Kiryukhin, S. G. Lee, and S. W. Cheong, Phys. Rev. B **65**, 144113 (2002).
[20] G. Shirane, J. D. Axe, and J. Harada, and A. Linz, Phys. Rev. B **2**, 3651 (1970).
[21] O. Delaire, J. Ma, K. Marty, A. F. May, M. A. McGuire, M-H. Du, D. J. Singh, A. Podlesnyak, G. Ehlers, M. D. Lumsden, and B. C. Sales, Nat. Mater. **10**, 614 (2011).
[22] J. Hlinka, S. Kamba, J. Petzelt, J. Kulda, C. A. Randall, and S. J. Zhang, Phys. Rev. Lett. **91**, 107602 (2003).
[23] B. Skinner, There's nothing particularly "spooky" about avoided crossing, https://gravityandlevity.wordpress.com/2014/04/08/avoided-crossing/ (2016).
[24] G. Xu, J. Wen, C. Stock, and P. M. Gehring, Nat. Mater. **7**, 562 (2008).
[25] S. Zhang and F. Li, J. Appl. Phys. **111**, 031301 (2012).
[26] M. E. Manley, D. L. Abernathy, R. Sahul, D. E. Parshall, J. W. Lynn, A. D. Christianson, P. J. Stonaha, E. D. Specht, and J. D. Budai, Sci. Adv. **2**, e1501814 (2016).
[27] W. Cochran, Phys. Rev. Lett. **3**, 412 (1959).
[28] H. Fu and R. E. Cohen, Nature (London) **403**, 281 (2000).
[29] T. Egami and S. J. L. Billinge, *Underneath the Bragg Peaks, Structural Analysis of Complex Materials*, edited by R. W. Cahn (Pergamon Materials Series, New York, 2003), p. 343.
[30] B. P. Burton and E. Cockayne, Phys. Rev. B **60**, R12542 (1999).

[31] D. L. Abernathy, M. B. Stone, M. J. Loguillo, M. S. Lucas, O. Delaire, X. Tang, J. Y. Y. Lin, and B. Fultz, Rev. Sci. Instrum. **83**, 15114 (2012).

[32] R. T. Azuah, L. R. Kneller, Y. Qiu, P. L. W. Tregenna-Piggott, C. M. Brown, J. R. D. Copley, and R. M. Dimeo, J. Res. Natl. Inst. Stand. Technol. **114**, 341 (2009).

[33] S. N. Gvasaliya, B. Roessli, R. A. Cowley, S. Kojima, and S. G. Lushnikov, J. Phys.: Condens. Matter **19**, 016219 (2007).

[34] H. Cao, C. Stock, G. Xu, P. M. Gehring, J. Li, and D. Viehland, Phys. Rev. B **78**, 104103 (2008).

[35] S. B. Vakhrushev and S. M. Shapiro, Phys. Rev. B **66**, 214101 (2002).

[36] A. Al-Zein, J. Hlinka, J. Rouquette, and B. Hehlen, Phys. Rev. Lett. **105**, 017601 (2010).

[37] M. Kempa and J. Hlinka, Phase Transitions **84**, 784 (2011).

[38] C. W. Li, O. Hellman, J. Ma, A. F. May, H. B. Cao, X. Chen, A. D. Christianson, G. Ehlers, D. J. Singh, B. C. Sales, and O. Delaire, Phys. Rev. Lett. **112**, 175501 (2014).